Nano Energy 98 (2022) 107338

Contents lists available at ScienceDirect

Nano Energy

journal homepage: www.elsevier.com/locate/nanoen

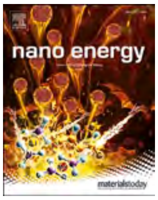

Synergistic modulation of local environment for electrochemical nitrate reduction via asymmetric vacancies and adjacent ion clusters

Dong Chen [a], Shaoce Zhang [a], Xiuming Bu [a], Rong Zhang [a], Quan Quan [a], Zhengxun Lai [a], Wei Wang [a,b], You Meng [a,b], Di Yin [a], SenPo Yip [c], Chuntai Liu [d], Chunyi Zhi [a], Johnny C. Ho [a,b,c,*]

[a] Department of Materials Science and Engineering, City University of Hong Kong, 999077, Hong Kong SAR, China
[b] State Key Laboratory of Terahertz and Millimeter Waves, City University of Hong Kong, 999077, Hong Kong SAR, China
[c] Institute for Materials Chemistry and Engineering, Kyushu University, Fukuoka 816-8580, Japan
[d] Key Laboratory of Advanced Materials Processing & Mold (Zhengzhou University), Ministry of Education, Zhengzhou 450002, China

ARTICLE INFO

Keywords:
Asymmetric oxygen vacancy
Mo cluster
Synergistic effect
Local environment
Electrochemical nitrate reduction

ABSTRACT

Electrochemical conversion of nitrate to ammonia is widely considered a “two birds with one stone” approach to alleviate the nitrate pollution in water and simultaneously to generate the valuable green NH_3 fuels. However, it remains challenging due to the lack of efficient electrocatalysts for practical utilization. Herein, we investigate the synergistic effect between asymmetric Cu-O_v-W sites (O_v represents oxygen vacancy) and adjacent Mo clusters in tuning the local electronic environment around active sites of catalysts for substantially enhanced nitrate reduction. The dynamic balance between the adsorption and desorption of O in NO_3^- caused by asymmetric O_v and the promoted protonation process due to Mo clusters are responsible for boosting the entire process. Such synergistic effect modulates the local electronic environment for binding the reaction intermediates and dramatically facilitates the intermediate formation in rate-determining steps (*NO→*NOH and *NOH→*N), leading to the high NH_3 Faradaic efficiency and yield rate of 94.60% and 5.84 mg h^{-1} $mg_{cat.}^{-1}$ at −0.7 V vs. RHE, respectively.

1. Introduction

Over the past several decades, the removal or conversion of nitrate (NO_x^- species) in agricultural sewage has been highly desired due to its severe damage to aquatic ecosystems, underground water and eventually poses a threat to human health [1–3]. Fortunately, ammonia (NH_3) plays a significant role in the nitrogen cycle and is a promising raw material of hydrogen-rich fuels in the industry [4]. At present, there are two typical pathways utilized to produce ammonia. The conventional Haber-Bosch process requires complicated chemical reactions between N_2 and H_2 implemented at high temperatures and pressures. In comparison, the electrochemical nitrogen reduction reaction (NRR) can be executed at ambient conditions, but it presents a 2–3 orders lower yield rate than the Haber-Bosch process [5,6]. To this end, the electrochemical nitrate reduction reaction (NO_3RR) can potentially convert NO_3^- to NH_3 under ambient conditions through the relatively low dissociation energy of N═O bond (204 kJ mol^{-1}) compared to that of N≡N bond (941 kJ mol^{-1}). The successful implementation of the electrochemical NO_3RR process would bring substantial economic and environmental impacts to different communities, regarded as a “two birds with one stone” approach to alleviate the nitrate pollution and simultaneously to generate the valuable green NH_3 fuels [7,8]. However, since the NO_3RR involves eight-electron transfer processes and is competitive with the undesired hydrogen evolution reaction (HER), it is urgent to explore electrocatalysts with high selectivity and Faradaic efficiency (FE) toward NH_3/NH_4^+ for its large-scale deployment [9].

It is well-known that the active sites and their local electronic environment are important factors dictating the activity of electrocatalysts. This way, defect engineering would play a vital role in improving their electrochemical performance because defects are generally considered as active sites, such as oxygen vacancies (O_v) [10,11]. Many state-of-art electrocatalysts have been demonstrated that the existence of O_v gives rise to an electronic-rich surface that lowers the adsorption/activation energy of the target molecule [12–14]. In contrast, the electrochemical

---

* Corresponding author at: Department of Materials Science and Engineering, City University of Hong Kong, 999077, Hong Kong SAR, China.
E-mail address: johnnyho@cityu.edu.hk (J.C. Ho).

https://doi.org/10.1016/j.nanoen.2022.107338
Received 22 December 2021; Received in revised form 19 April 2022; Accepted 29 April 2022

performance is not always monotonously related to the concentration of O_V. Still, it is dominated by a dynamic equilibrium between the formation and the vanish of O_V [15]. This phenomenon is possibly the result that O_V sometimes is unstable upon highly oxidized and oxygen-rich environments [16]. Recently, it has been suggested that the site symmetry of O_V has a particular impact on the catalytic activity of materials. Specifically, a symmetric O_V represents the site chained with the symmetric coordinated cations, whereas the linkage terminals of ones constituted by different kinds of cations are called “asymmetric O_V” [17]. The latter is demonstrated to keep a dynamic balance between the adsorption and the desorption of oxygen species, leading to the molecular “easy come, easy go” tactic. According to the Sabatier principle, the balance between the binding strength of the reactants, intermediates and products is paramount to catalytic activity, i.e., strong enough to adsorb and weak enough to desorb [18]. Since NO_3RR involves both the adsorption and the desorption of O, such asymmetric O_V is valuable to be investigated.

Furthermore, polyoxometalates (POMs) are a large group of transition metal-oxygen anionic polynuclear clusters that possess rich hollow sites that could easily anchor on foreign metal ions [19]. These transition metal clusters with bridged metal-metal interactions can minimize the distance between single-atom centers, further improving the intrinsic activity and stability compared to single-atom catalysts (SACs) and maximizing the efficiency of metal atoms utilization compared to metal particles [20,21]. Moreover, the metal ions usually have the unoccupied d-orbitals, which can accept multiple electrons, resulting in the modulation of charge transfer when binding to NO_3^- [22]. In this case, although there are several individual works focused on the O_V-promoted and ion clusters-promoted electrocatalysis, respectively, there are very few emphasis on their combined effect on the electrochemical performance of catalysts. Particularly, because of the dynamic adsorption equilibrium for oxygen species of the aforementioned asymmetric property of O_V, such vacancies would also serve as favorable sites to attract and then disjoint oxygen atoms in POMs, leading to the loading of transition metal ion clusters on the fixed position. Inspired by these characteristics, it is anticipated that the ion clusters can be placed

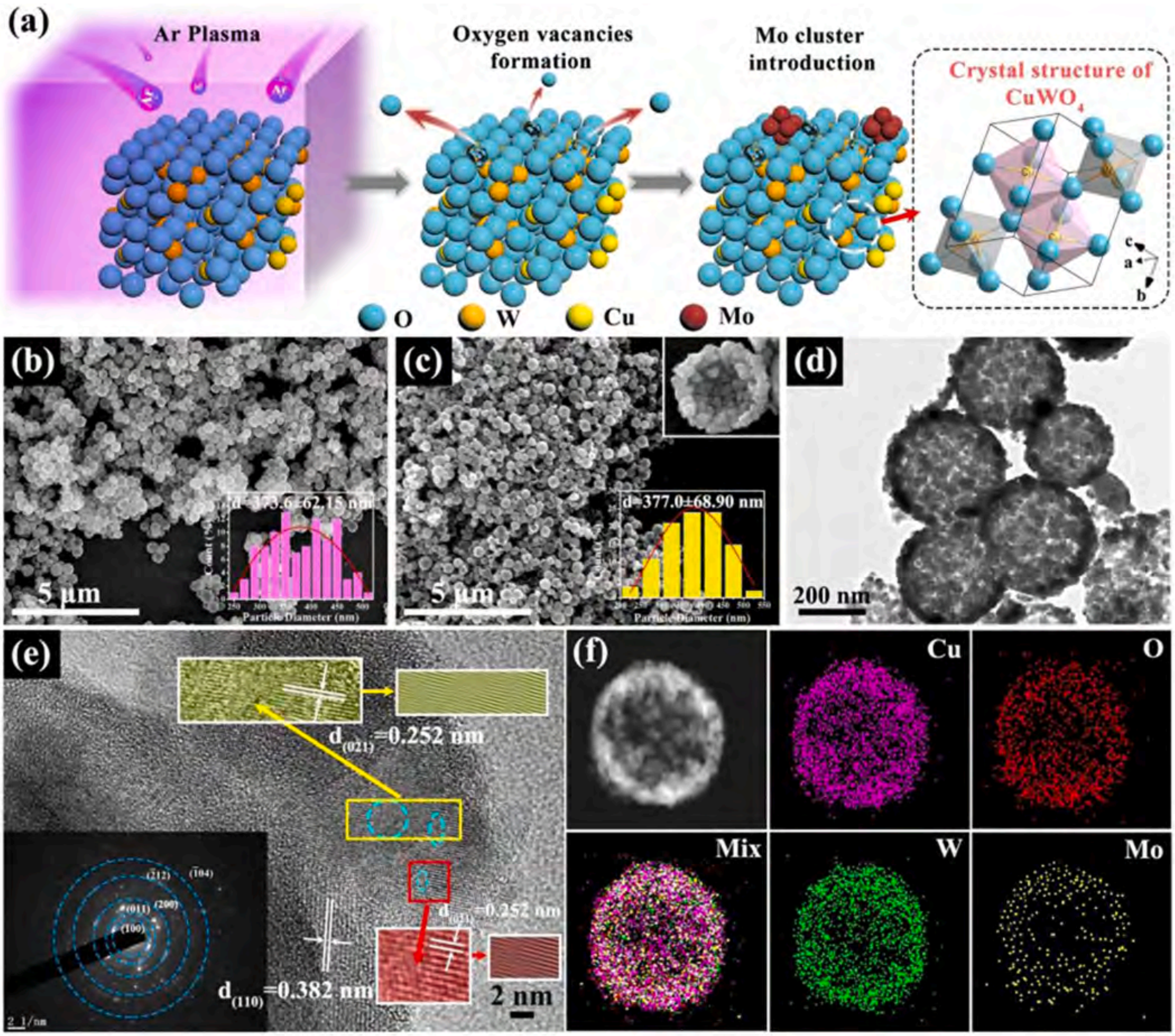

Fig. 1. (a) Schematic illustration of the fabrication procedure for Mo/H-CuW. (b) SEM image of CuW. (c-f) SEM image, TEM image, HRTEM image, STEM image, and the corresponding STEM-EDS elemental mapping images of Mo/H-CuW. The insets in (b, c) are the particle size distribution. The inset on the lower left in (e) is the SAED pattern of Mo/H-CuW, and the red and yellow boxes are the amplifying HRTEM and the corresponding IFFT images from the circled regions.

close to the asymmetric O_v to form active trimer sites for NO_3RR.

Herein, we are the first team to report the synergistic effect of asymmetric O_v and Mo clusters on the copper tungstate ($CuWO_4$) hollow nanospheres for highly efficient NO_3RR. To be specific, a gas (Ar or O_2) plasma treatment is employed to induce different concentrations of asymmetric Cu-O_v-W sites. By accurately locating the Mo cluster close to the asymmetric O_v, one can act as an electron donor to promote the adsorption/desorption of O in NO_3^- while another holds the post of charge-compensating role to accept electrons expediting the protonation process. All these processes can effectively modulate the local environment of active sites for enhanced NO_3RR performance. It is impressive that this synergistic effect could contribute to a high FE of 94.6% and a good yield rate of ammonia of 5.84 mg h^{-1} $mg_{cat.}^{-1}$ at − 0.7 V vs. RHE. DFT calculations further revealed the higher adsorption energy of NO_3^- and the lower energy of rate-limiting step for the reduction process by asymmetric O_v and adjacent Mo clusters. This work highlights the synergistic effect of asymmetric O_v and ion clusters in promoting NO_3RR performance, providing a novel strategy for engineering the local environment around active sites of electrocatalysts.

2. Results and discussion

The fabrication procedure for Mo clusters decorated $CuWO_4$ hollow nanospheres with a high concentration of asymmetric O_v (denoted as Mo/H-CuW) is displayed in Fig. 1a. In detail, the $CuWO_4$ hollow nanospheres (CuW HNS) were first synthesized by a facile hydrothermal method, followed by thermal treatment (Fig. S1). The morphology of $CuWO_4$ is dominantly dictated by the duration of the hydrothermal process (Figs. S2 and S3). With the increasing duration from 6 h to 48 h, the size of nanospheres was found to increase from ~ 305 nm to ~372 nm, experiencing three different postures: solid nanospheres, hollow nanospheres, and eventually broken spheres. Then, we introduced various concentrations of O_v into CuW by controlling the plasma atmosphere (O_2 or Ar). When Ar plasma bombards the surface of CuW, the internal energy of metastable Ar-plasma can be transferred to the surface atoms, leading to the removal of the relatively light oxygen atoms [23]. In contrast, the O_2 plasma-induced oxygen ions or radical groups were trapped inside CuW to fill O_v, and hence producing CuW with high and low concentrations of O_v, respectively (donated as H-CuW and L-CuW). The inset in Fig. 1a shows the typical structure of a triclinic CuW crystal, constituted by two distorted octahedral [CuO_6] and [WO_6] clusters, respectively. Every O atom is linked to at least one W and one Cu atom. Such property is greatly in accord with that of asymmetric sites, which own two opposite influences from at least two surrounding cations with different electronegativity, facilitating or hindering the production of O_v [24]. Such Cu-O_v-W sites are anticipated to act as the highly active sites for NO_3RR. The Fourier-transform infrared spectroscopy (FT-IR) spectra displayed in Fig. S4 demonstrate the transformation from $Cu_2WO_4(OH)_2$ precursor to $CuWO_4$ during the thermal treatment. Apart from the band located at around 470 cm^{-1}, representing the symmetric stretching vibrations of [CuO_6] (Fig. S4b), the other peaks (908, 710, 554 and 420 cm^{-1}) belong to the symmetric stretching, anti-symmetric stretching (Fig. S4c), interactive symmetric stretching and symmetric bending vibrations of the distorted [WO_6] clusters, accordingly [25]. This information proves the distortions on octahedral [CuO_6] and [WO_6] clusters and further suggests the degree of asymmetry Cu-O_v-W sites. Making use of the function of asymmetric O_v that balances the adsorption and desorption of oxygen species, POM (ammonium paramolybdate) as Mo source was introduced into H-CuW and L-CuW to orientate the Mo cluster next to the O_v (latter donated as Mo/L-CuW). After that, the oxygen atoms trapped in the vacancy sites were removed through reduction under H_2/Ar atmosphere at a low temperature. The SEM images (Figs. 1b, c and S5) depict the CuW shape as hollow nanospheres with the shell composed of numerous particles. After experiencing the O_2/Ar plasma, there is no apparent change happened to the morphology (Fig. S5). The clear dark and light boundaries are clearly observed in the TEM images (Figs. 1d and S6a), further confirming the hollow structure of the materials. It is well-known that such kinds of hollow-structured nanomaterials generally have larger specific surface areas than the solid ones, thereby enabling the exposure of more active sites and promoting electrocatalytic activity [26,27]. More importantly, there are more interfaces among the thin shells because of the numerous small particles of the CuW HNS, which provides fast channels for mass transport. Based on the HRTEM images (Figs. 1e and S6b), the lattice fringes with the interplanar spacings of 0.310 nm, 0.382 nm and 0.252 nm are witnessed and corresponded to the ($\overline{1}\overline{1}1$) (110) and ($0\overline{2}1$) planes of triclinic CuW, respectively. It is noteworthy that most of the lattice fringes are inconsecutive in the images of Mo/H-CuW. After applying the inverse fast Fourier transform (IFFT) on the selected region, there are obvious dislocations and distortions observed, further indicating the introduction of abundant defects into the lattice due to the plasma treatment and Mo doping. These defect generations would enable the substantial increment of active sites, which would be proved by the following experiments [28,29]. The SAED pattern (inset of Fig. 1e) suggests the characteristics of polycrystalline triclinic CuW. The scanning transmission electron microscopy (STEM) shown in Fig. 1f and the corresponding elemental mapping images of Cu, W, O, and Mo imply that all elements distribute homogeneously throughout the HNS. Additionally, the existence of Mo constituents could also be identified by energy dispersive spectroscopy (EDS) and corresponding elemental mapping in Figs. S7 and S8. All these findings demonstrate the successful synthesis of Mo/H-CuW with large amounts of O_v.

Moreover, XRD is performed on all the samples and the collected patterns are shown in Fig. 2a. It is observed that all the samples are indexed to triclinic phase $CuWO_4$ (JCPDS no. 72–0616) without any other detectable impurities. In order to evaluate the various O_v concentrations in the samples, EPR, Raman and XPS measurements were carried out. As presented in Fig. 2b, there are obvious signals located at g = 2.002 observed, suggesting the presence of oxygen vacancies [30]. Interestingly, the pure CuW displays the same EPR signal, which indicates that the CuW also possesses the defects. These disparate intensities of the signal prove the different concentrations of O_v in H-CuW and L-CuW. At the same time, the high-resolution XPS spectra of O 1 s are displayed in Fig. 2c. There are two peaks positioned at about 530.2 eV and 531.2 eV, which can be assigned to lattice oxygen (B) and oxygen atoms next to O_v (A) [31]. The higher ratio of A/B of H-CuW compared to others intuitively demonstrates the higher concentration of O_v upon the bombardment of Ar-plasma. As depicted in the Raman spectra in Fig. 2d, the Raman bands are assigned to the Raman-active vibrational modes (A_g) of triclinic $CuWO_4$. Compared with L-CuW and CuW, the Raman bands of H-CuW are weaker and broader, indicating the decrease of (O-Cu-O)/(O-W-O) bonds and the generation of more O_v in CuW [32,33]. Therefore, the above measurements reveal that the Ar-plasma yields numerous O_v defects in the CuW HNS, while the O_2-plasma removes the O_v. Meanwhile, the Cu 2p and W 4f XPS spectra are shown in Fig. S9. Both the peaks of Cu 2p and W 4f shift to the lower binding energy with the increasing O_v concentration. Such negative shifts indicate the increase of the local electron density of Cu and W due to the offer of delocalized electrons in the O_v. This way, the obtained Cu-O_v-W asymmetric sites are expected to modulate the local charge distribution and then contribute to polarizing the adsorbed NO_3^- molecules for better activation and surface electrochemical nitrate reduction process [34]. After introducing the Mo clusters into H-CuW and L-CuW, the peaks of Mo 3d appear and become stronger in the XPS survey spectra as given in Fig. 2e. It is found the peaks of Cu $2p_{3/2}$ and Cu $2p_{1/2}$ locate at a similar position by comparing Mo/H-CuW and Mo/L-CuW to H-CuW and L-CuW, respectively (Figs. 2f and S9a). However, the peaks of W 4f of Mo/H-CuW are observed to shift to higher binding energies (Fig. 2g). Such results confirm the electron transfer from W to Mo clusters and the formation of W-O-Mo bonds with the help of Cu-O_v-W asymmetric sites. As aforementioned, the POM molecules possess rich

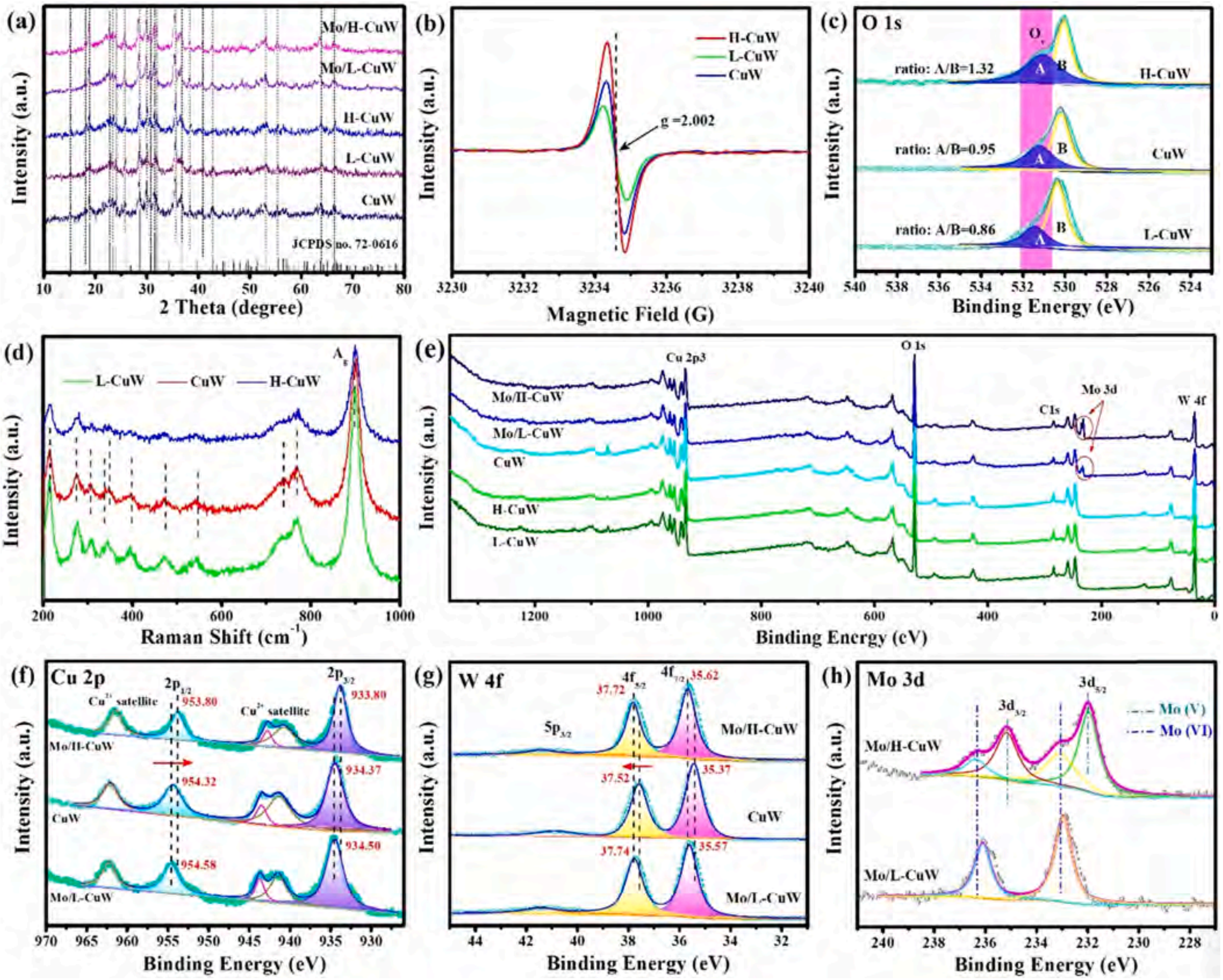

Fig. 2. Characterizations of (a) XRD patterns, (b) EPR spectra, (c) O 1s XPS spectra, (d) Raman spectra, (e) XPS survey spectra. (f-h) Cu 2p, W 4f and Mo 3d XPS spectra for the as-obtained samples.

hollow sites that are capable of adsorbing foreign metal ions. Because of the similar valance state and electronegativity between W and Mo, the Mo-based POMs prefer to bond with W. But the minor degree of shift of Mo/L-CuW compared to Mo/H-CuW may be attributed to the relatively small amount of adsorbed Mo owing to the electron-barren environment and the fewer O_v sites. This is also demonstrated by the element content measured by XPS spectra, for that Mo contents in the Mo/L-CuW and Mo/H-CuW are determined to be 0.88 at% and 1.97 at%, respectively (Fig. S10). In the Mo 3d XPS spectra of Mo/H-CuW, the deconvoluted peaks at 232.04 eV, 235.16 eV and 233.07 eV, 236.33 eV can be indexed to Mo^{5+} and Mo^{6+}, respectively, whereas only Mo^{6+} exists in the sample of Mo/L-CuW (Fig. 2h). As for the VI valence state of Mo in the pristine POMs, the V valence state may be resulted from the charge transfer along with the W-O-Mo bonds [35]. The O 1s spectra and the EPR tests in Fig. S11 further confirm that the concentration of O_v remains nearly constant after the introduction of Mo clusters. As a result, all these results clearly demonstrate the successful formation of plasma-regulated Cu-O_v-W asymmetric sites and accurately located Mo clusters in $CuWO_4$. By combining the electron-donating O_v and the electron-compensating Mo cluster, such electrocatalyst is expected to have substantially enhanced and stable electrochemical activity.

To shed light on the synergistic effect of O_v and Mo clusters towards NO_3RR performance, a two-compartment H-type electrolytic cell was constructed with its characteristics evaluated under ambient conditions. The LSV curves are measured in the Na_2SO_4 electrolyte with and without NO_3^- as shown in Fig. 3a. The current densities of all the samples for NO_3RR are distinctly higher over a wide range of negative potentials than the ones for HER, indicating the electrocatalytic activity for NO_3^- reduction and the poor activity on HER, which enables the high selectivity for NH_3 production. Besides, the LSV curves in Fig. S12 demonstrate the superiority of hollow-structured CuW (prepared for 24 h) compared with both the solid (6 h) and broken (48 h) ones owing to the much more exposed active sites and faster charge transfer channels. To obtain the NH_3 yield rate and FE, a series of controlled-potential CA measurements are carried out in NO_3^--contained electrolyte. As anticipated, H-CuW HNS achieves the highest NH_3 FE of 75.61% with a yield rate of 3.63 mg h^{-1} $mg_{cat.}^{-1}$ at − 0.70 V vs. RHE (Figs. 3b and S13), significantly outperforming L-CuW (FE of 41.63% and yield rate of 1.63 mg h^{-1} $mg_{cat.}^{-1}$) and CuW HNS (FE of 49.25% and yield rate of 2.14 mg h^{-1} $mg_{cat.}^{-1}$). It is worth mentioning that the highest FE of H-CuW appears at a more positive potential than the counterparts, which means it only needs a smaller voltage to achieve the higher NO_3^- reduction efficiency, emphasizing the remarkable selectivity of CuW with high concentration of O_v sites. To obtain further insights, we performed DFT calculations to obtain the partial density of states (PDOS) of H-CuW and L-CuW. In Fig. 3d and e, the d-band centers of H-CuW and L-

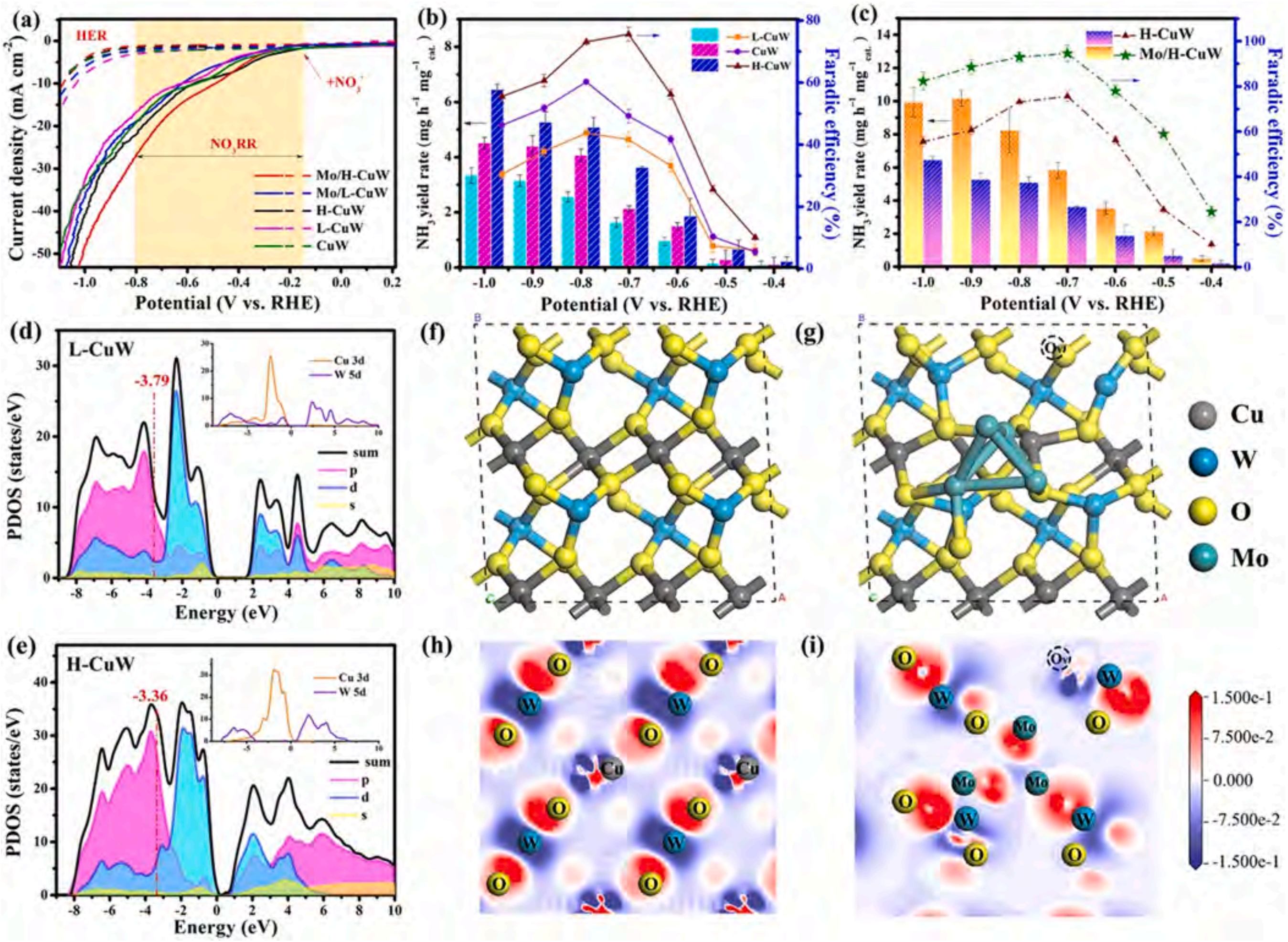

Fig. 3. (a) LSV curves of Mo/H-CuW, Mo/L-CuW, H-CuW, L-CuW, and CuW in 0.5 M Na_2SO_4 electrolyte with and without NO_3^- upon a scan rate of 5 mV s^{-1}. (b) NH_3 yield rate and Faradaic efficiency of L-CuW, CuW, and H-CuW. (c) NH_3 yield rate and Faradaic efficiency of H-CuW and Mo/H-CuW. (d) PDOS of L-CuW. (e) PDOS of H-CuW. (f, g) Optimized L-CuW and Mo/H-CuW structures along (010) plane. (h, i) The corresponding electron contour maps of the (010) slice in (f) and (g).

CuW are determined to be − 3.36 eV and − 3.79 eV, which infers that the d-band center would be closer to the Fermi energy with the increasing O_v concentration. According to the d-band theory, the d-band center location can be considered a good descriptive tool for estimating the adsorbate-metal electronic interaction [36]. Hence, the upshift of the d-band center demonstrates the crucial function of Cu-O_v-W sites in modulating the local environment toward the adsorption of NO_3^-, thus weakening and activating the N=O bond. After that, in connection with the effect of potential change, the NH_3 yield rate of Mo/H-CuW gradually increases as the reduction potential increases from − 0.4 V to − 1.0 V, offering the NH_3 yield rate of 5.84 mg h^{-1} mg$^{-1}_{cat.}$ at − 0.7 V vs. RHE (Fig. 3c). The highest FE reaches 94.60% at − 0.7 V vs. RHE, surpassing those of H-CuW and L-CuW by a factor of 1.25 and 2.27, respectively. Such performance is comparable and even superior to most of the state-of-the-art electrocatalysts reported on NO_3RR (Table S1). The NH_3 yield rate is several orders of magnitude higher than that of electrocatalysts reported in NRR, further indicating the superiority of NO_3RR for NH_3 production. Furthermore, the decreased FE at higher potentials could be attributed to the progressively enhanced competing HER. From the comparisons of NH_3 yield rate and FE depicted in Fig. S14, we find that the best performance of Mo/L-CuW only arrives 59.86% at − 0.7 V vs. RHE and 4.48 mg h^{-1} mg$^{-1}_{cat.}$ at − 1.0 V vs. RHE, which are close to the values of CuW but higher than that for L-CuW. These results suggest that even with a low content of Mo, the Mo/L-CuW show the promoted NO_3RR activity compared to L-CuW, implying that Mo clusters play a critical role in the reduction process. Since Mo has been demonstrated as an active site for nitrate reductase of biogeochemical cycles, it is probable to speculate that the Mo site also works for NO_3RR [37]. More importantly, the catalytic activity has a significant correlation with the d-band electronic structure of active atoms exposed on the surface. The Mo atoms with unoccupied d-orbitals can accept electrons from the π*-orbital of NO_3^-, strengthening the adsorption of N in NO_3^- consequently [38]. Therefore, we can conclude that the combination of asymmetric O_v and Mo clusters serves as a tool with multiplying effect to modulate the local electronic environment of active sites for NO_3RR activity.

DFT calculations were further wielded to demonstrate the remarkable NO_3RR activity of Mo/H-CuW. Fig. 3f and g give the optimized L-CuW and Mo/H-CuW structures along the (010) plane while Fig. 3h and i display the corresponding electron contour maps, which intuitively give the information of electron distribution. The indigo blue and red regions designate the depletion and accumulation of charge density, respectively. We found that strong electronic interactions exist in the W-O and Cu-O bonds, implying the presence of abundant electron transport channels [39]. Meanwhile, the W-O-Cu region surrounded with lop-sided electronic distribution further proves the asymmetric individuality formed due to the different electronegativity and distortion of [WO_6] and [CuO_6] octahedrons. In Mo/H-CuW, with Cu-O_v-W asymmetric sites and adjacent Mo clusters, the electron accumulation cloud around O_v transfers to the W atom in the visual area, representing more electrons to move from vacancy to the sides. Also, the large electron clouds gather around the Mo cluster area, which implies the strong interaction of the Mo cluster with the surrounding environment. Such electron transfers better modulate the electronic structure and local environment around active sites. These abundant electrons and strong interactions will trigger the substantial back donation to the antibonding $^*NO_3$ (where * represents the active site on the catalyst surface) orbitals after NO_3^- adsorption to promote the subsequent NO_3RR activity [40]. The above results are in good agreement with that of XPS spectra. Therefore, it is believed that the enhanced NO_3RR performance of Mo/H-CuW depends heavily on the synergetic effect of optimal d-band center and unsaturated coordination bonds of asymmetric O_v, as well as the electron receiving and back donation of Mo clusters.

Since NO_2^- is one of the important by-products in NO_3RR, and NO_3^--to-$^*NO_2$ conversion is the rate-determining step (RDS) in some previous works [41], it is essential to detect the concentration of NO_2^- in the electrolyte. As shown in Figs. S15 and S16, both L-CuW and Mo/H-CuW display the higher FE of NO_2^- than NH_3 at a lower voltage, indicating the faster kinetics of the NO_3^--to-$^*NO_2$ conversion process to desorb NO_2^- as a by-product. Remarkably, with the increasing applied voltage, the FE of NH_3 gets gradually strengthened while that for NO_2^- is greatly suppressed, suggesting the dynamic equilibrium for NO_2^- production [42]. In detail, due to the fast reaction at the beginning of NO_3RR, more NO_2^- are broken away from the surface of the catalyst rather than be reduced to NH_3. However, when it reaches a dynamic equilibrium, the yield of NO_2^- will be controlled at a certain level, and then participate in the subsequent reaction with the increasing voltage, enabling the $^*NO_2$-to-NH_3 conversion process. In addition, there are two important points needed to be emphasized. The first one is the location of FE intersection of between NO_2^- and NH_3 for Mo/H-CuW taking place at a lower voltage compared to that of L-CuW, demonstrating the higher selectivity towards NO_3^--to-NH_3 than NO_3^--to-$^*NO_2$. The other is the decreasing total FE ($NO_2^- + NH_3$) for L-CuW, which indicates that the competing HER starts to gradually occurred at the higher potentials, agreeing well with the LSV results discussed above. In any case, as anticipated, the total FE for Mo/H-CuW maintains at a high value of over a wide range of voltage window, indicating the ability to suppress the generation of H_2. More importantly, since no N_2H_4 was detected in the electrocatalytic process on Mo/H-CuW, indicating that the majority product is NH_3 in our work (Fig. S17).

Apart from the catalytic activity and selectivity, stability is another critical performance indicator of electrode materials. In this work, we perform a series of measurements to evaluate the stability of Mo/H-CuW. Since the NH_3 FE for H-CuW shows an apparent descending tendency after 15 cycles compared to the one of L-CuW (Figs. 4a and S18), it is inferred that the reduction is caused by the fugitiveness of O_v [30]. Although the asymmetric O_v could theoretically balance the adsorption/desorption of O in NO_3^-, the practical experiments of H-CuW indicate that it has a relatively slow kinetic for the eight-electron transfer reduction process. Thus, less and less O_v is left to absorb additional NO_3^- due to the fugitiveness as the number of cycles increases. However, when loading the Mo clusters onto H-CuW, the NH_3 FE fluctuates but still maintains at around 90%, consolidating the significance of the synergistic effect between asymmetric O_v and Mo clusters. In previous works, many researchers found the bridge or hollow site adsorption available on the Mo metal surface for the strong *N binding strength and relatively stable *H [38,43,44]. Therefore, this synergistic effect could not only promote the NO_3RR/HER selectivity but also accelerate the protonation steps in NO_3RR. This is why the O_v-only H-CuW displays the decreasing efficiency after repetitive use, but the Mo/H-CuW does not. We also evaluate the NH_3 concentration for a consecutive 120 h of NO_3RR by extracting the desired electrolyte at specific time points (with catalyst loadings of 0.25 mg). Here, the concentration of NH_3 for Mo/H-CuW reaches 42.44 mM after 120 h. Both H-CuW and Mo/H-CuW show the increasing yields of NH_3 but these increasing yield rates start to slow down and tend to saturate after 72 h (Fig. 4b). Combined with the stability results presented in Fig. 4a, H-CuW and Mo/H-CuW have different reasons for their gradually reduced increasing yield rates of

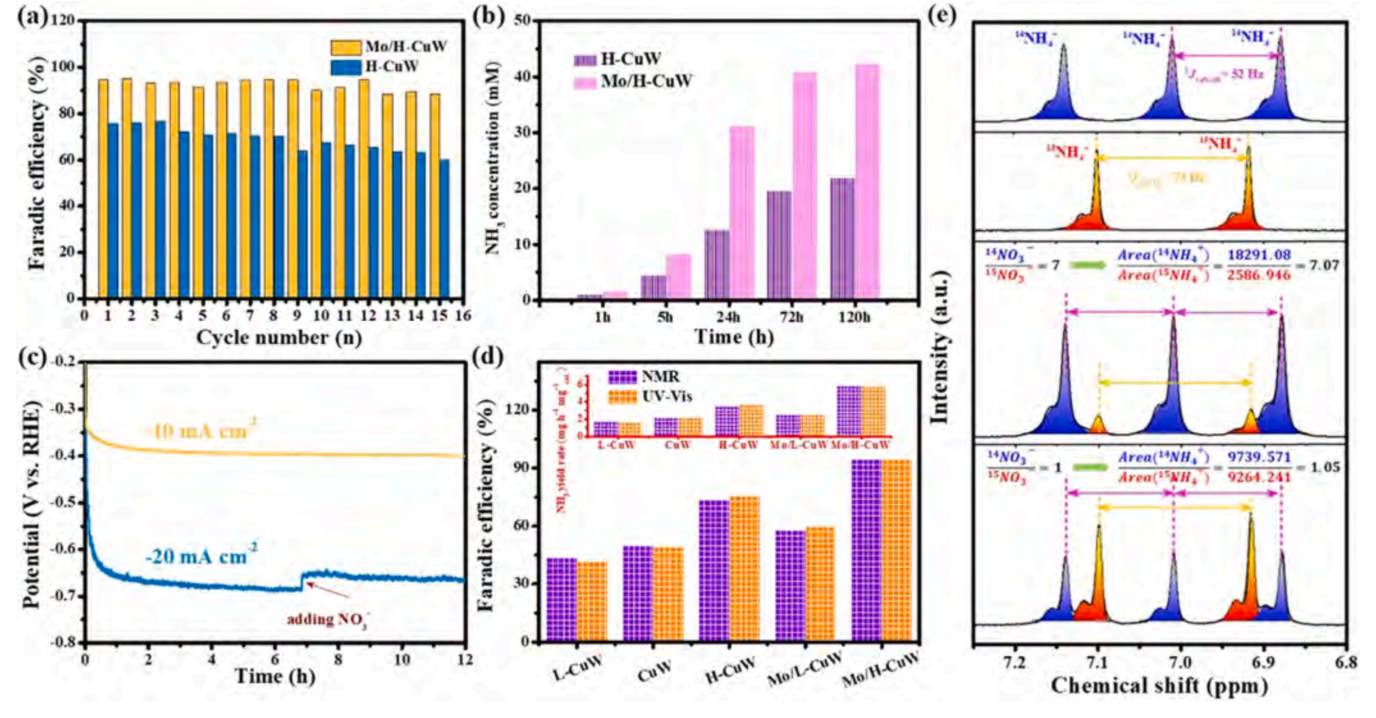

Fig. 4. (a) NH_3 Faradaic efficiency in consecutive cycling tests on Mo/H-CuW and H-CuW. (b) NH_3 concentration after consecutive 120 h reaction of Mo/H-CuW and H-CuW. (c) Chronopotentiometry test of Mo/H-CuW at the current density of − 10 and − 20 mA cm^{-2} over 12 h. The tests in (a-c) were all conducted in 0.5 M Na_2SO_4 electrolyte with 0.05 M NO_3^-. (d) The quantitative comparison of the NH_3 yield rate and Faradaic efficiency of the samples based on the ^1H NMR and UV-Vis method. (e) The ^1H NMR spectra of standard $^{14}NH_4^+$ and $^{15}NH_4^+$, and obtained $^{14}NH_4^+$ and $^{15}NH_4^+$ from NO_3RR with different ratios of $^{14}NO_3^-/^{15}NO_3^-$ as feed. All electrodes were measured at − 0.7 V vs. RHE.

NH_3. For the case of H-CuW, there is a decline in the increasing yield rate of NH_3 owing to the dissipation of unstable O_v as the reaction keeps going on. On the other hand, Mo/H-CuW has a slowing-down increasing yield rate of NH_3 because of the rapid depletion of limited NO_3^- in the electrolyte such that the reduction of NO_3 is close to saturation. This fast consumption of NO_3^- can as well be illustrated by the increasing potentials required to maintain stable current densities of -10 and -20 mA cm^{-2} for Mo/H-CuW (Fig. 4c). Notably, when additional NO_3^- is added into the electrolyte, the potential can be recovered to its initial value for the large current density of -20 mA cm^{-2}, further confirming the rapid depletion of NO_3^- during the reaction as well as the prominent NO_3^- reduction kinetics of Mo/H-CuW [45]. Moreover, the samples constructed with a high concentration of O_v are observed to exhibit the greater values of electrochemically active surface area (ECSA), suggesting the presence of more active sites in the electrodes (Fig. S19). In particular, Mo/H-CuW has a NH_3 yield rate of 1.83 mg h^{-1} mg$_{cat.}^{-1}$ mF cm^{-2} after normalization, which is remarkably higher than those of L-CuW (0.94 mg h^{-1} mg$_{cat.}^{-1}$ mF cm^{-2}), CuW (1.01 mg h^{-1} mg$_{cat.}^{-1}$ mF cm^{-2}), H-CuW (1.22 mg h^{-1} mg$_{cat.}^{-1}$ mF cm^{-2}) and Mo/L-CuW (1.36 mg h^{-1} mg$_{cat.}^{-1}$ mF cm^{-2}), which indicates that Mo/H-CuW does not only have a large ECSA value but also comes with the more active intrinsic properties. Also, the relatively large ECSA value of H-CuW and the high normalized NH_3 yield rate of Mo/L-CuW further suggest that the O_v can be exploited as active sites, whereas the Mo clusters are the primary factor for the improvement of intrinsic activity, perfectly agreeing with the analysis discussed above. Based on the Nyquist plot and the equivalent circuit diagram as shown in Fig. S20, the charge transfer resistance (R_{ct}) of Mo/H-CuW, H-CuW, Mo/L-CuW and L-CuW can be fitted well to the circuit model and determined to be 6.50, 9.75, 11.36 and 18.20 Ω, respectively, where the smallest R_{ct} of Mo/H-CuW demonstrates the efficient charge transfer in the electrode. More importantly, the steepest slope of Mo/H-CuW related to Warburg impedance in the low-frequency region implies the fastest ion diffusion kinetics in the electrode/electrolyte, confirming again the improved electrical conductivity and rapid mass transfer capability with the assistance of asymmetric O_v and Mo clusters [46,47]. To trace the source of the obtained NH_3, we detected the NH_3 yield rate in 0.5 M Na_2SO_4 without NO_3^-, in which the NH_3 yield rate is negligible. This result indicates that there is no nitrate in the Na_2SO_4 electrolyte, affecting the electrocatalytic process (Fig. S21). At the same time, isotope labeling tests using ^{1}H NMR are then performed with the results compiled in Fig. 4d and e. With $^{15}NH_4^+$ as the feed and $C_4H_4O_4$ as the internal standard, the integrated peak area of $^{15}NH_4^+/C_4H_4O_4$ is directly related to the concentration of NH_3. By quantitatively comparing with the calibration curve (Fig. S22), the NH_3 yield rates and FEs based on the NMR and UV-Vis methods are nearly equal, evidently indicating that the obtained NH_3 originated from the electrocatalytic reduction of $^{15}NO_3^-$ instead of the ambient ammonia pollution. Furthermore, the triple and doublet patterns with the coupling constant of 52 Hz and 73 Hz are corresponded to the signals of $^{14}NH_4^+$ and $^{15}NH_4^+$, respectively (Fig. 4e). By adding a different ratio of $^{14}NO_3^-/^{15}NO_3^-$ (e.g., 7 and 1), the resultant ratio of $^{14}NH_4^+/^{15}NH_4^+$ after the electrocatalytic reduction process remains almost unchanged (i.e., 7.07 and 1.05). This different method once again identifies more accurately the source of ammonia as coming from the reduction process here.

Next, we perform DFT calculations to unveil the reaction mechanism of enhanced NO_3RR performance with the help of asymmetric O_v and Mo clusters in CuW. Firstly, the calculated Gibbs free energies towards the adsorption of $^*NO_3$ on the O_v site of H-CuW ($\Delta G = 2.41$ eV) and Mo/H-CuW ($\Delta G = 2.51$ eV) are found to be much higher than the one of Cu/W site in L-CuW, which proves that O_v is the optimal active site for binding NO_3^- (Fig. 5a). Figs. S23–S25 display the optimized geometric structure of the intermediates adsorbed on L-CuW, H-CuW and Mo/H-CuW substrates, respectively. Upon the adsorption of NO_3^-, the transfer of multiple protons and electrons takes place. All these three samples show the downhill energy for the first three reactions, revealing that the N=O bonds of $^*NO_3$ are spontaneously cleaved to $^*NO_2$ and $^*NO$ in a step-by-step manner. Taking Mo/H-CuW as an example (Fig. 5b), one of the O atoms fill the vacancy with unsaturated coordination, and Mo with the unoccupied d-orbital accepts the electron from π*-orbital of $^*NO_3$,

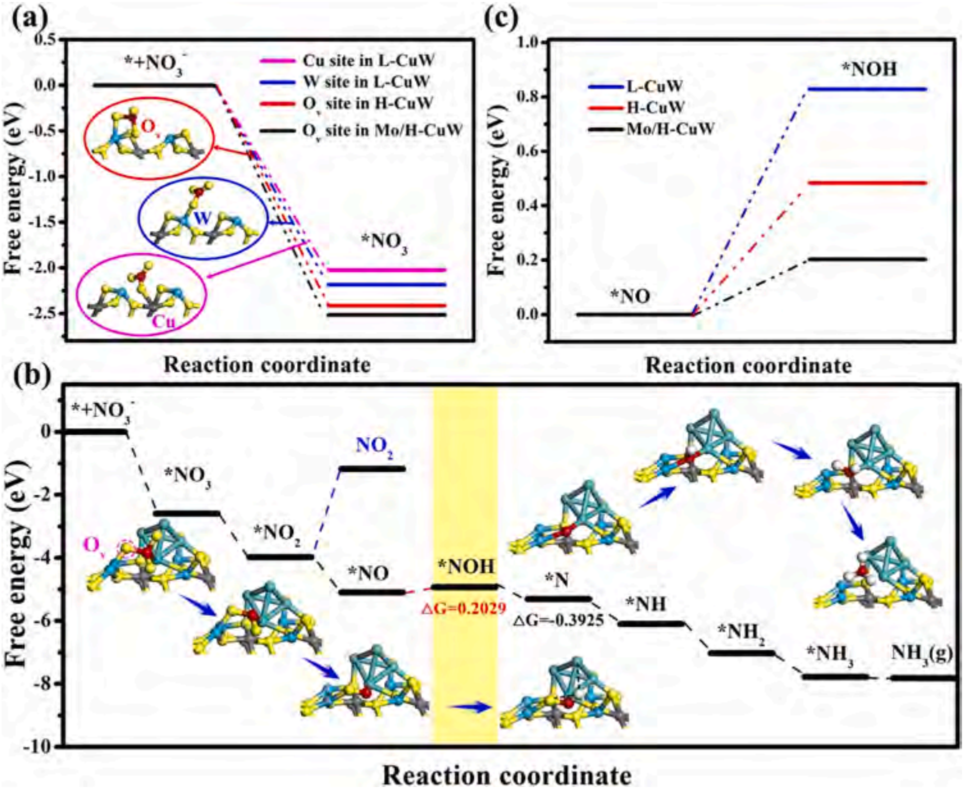

Fig. 5. (a) Calculated Gibbs free energy of the adsorption $^*NO_3$ on Cu or W site in L-CuW, O_v site in H-CuW and O_v site in Mo/H-CuW. The insets show typical structures of absorbed NO_3^- on different sites. (b) Calculated Gibbs free energy profiles of NO_3RR procedures on Mo/H-CuW and the corresponding optimized geometric structure of intermediates adsorbed on the substrate. (c) The comparison of the Gibbs free energy change in the rate-determining step of NO_3RR for L-CuW, H-CuW and Mo/H-CuW. Yellow, blue, gray, cyan and red spheres represent the O, W, Cu, Mo and N atoms, respectively.

and then bonds with N. Afterwards, $*NO_3$ attacks two proton-electron pairs to take off two O atoms. From the step of *NO to *NOH, the uphill energy change suggests that it is the rate-determining step in NO_3RR. Fig. 5c shows the comparison of RDS of the samples by setting the free energy of *NO as the standard. The ΔG of Mo/H-CuW is calculated to be 0.28 eV and 0.62 eV lower than those of H-CuW and L-CuW, demonstrating a more favorable reduction reaction in this system and being consistent with the experimental results. In the next step, only L-CuW shows a RDS (*NOH→*N) there. These results give two pieces of important information and further prove the synergetic effect of asymmetric O_v and Mo clusters. One is the relatively strong protonation process caused by Mo, which is derived from the small ΔG in the first RDS in Mo/H-CuW. The other is the easier desorption of O filled in asymmetric O_v confirmed by *NOH→*N in H-CuW and Mo/H-CuW change from endothermic to exothermic; thus, the reduction activity becomes much easier, promoting NH_3 yield rate and FE. Afterwards, the *N is hydrogenated to form *NH, $*NH_2$ and $*NH_3$, then gets released from the surface. It is noteworthy that the ΔG in the protonation process for Mo/H-CuW is 0.88 eV (taking $*NH \rightarrow *NH_2$ as an example), which is smaller than the other two counterparts (1.12 eV and 1.06 eV), further proving the good ability toward attracting active H radical of Mo clusters. Meanwhile, the electron-rich area around O_v/Mo demonstrated by the aforementioned PDOS and XPS results greatly guarantee the demanded electrons. Therefore, taking together the computational and experimental results, it is evident that the synergism between asymmetric O_v and Mo clusters can effectively modulate the local electronic structure of electrocatalysts for the efficient nitrate reduction to ammonia.

3. Conclusion

In summary, we report a facile strategy to fabricate asymmetric O_v along with adjacent Mo clusters. These two species are demonstrated to play a remarkable synergistic effect in tuning the local electronic environment around the active site and promoting the entire process of nitrate reduction. To be specific, the Ar plasma-induced high concentration of asymmetric Cu-O_v-W sites keep a dynamic balance between the adsorption and desorption of O in NO_3^-, leading to the molecular “easy come, easy go” tactic. Meanwhile, the upshift of d-band centers indicates the role of O_v in acting as active sites to absorb NO_3^- and weaken the N═O bond. This directly speeds up the reduction activity from *NOH to *N, which is initially an endothermic process in L-CuW. Moreover, Mo clusters play the charge-compensating role in accepting unpaired electrons in NO_3^- and accelerating the protonation process, leading to the decreased energy in the RDS of Mo/H-CuW. It is impressive that the Mo/H-CuW can reach a high NH_3 FE and yield rate of 94.60% and 5.84 mg h^{-1} $mg_{cat.}^{-1}$ at − 0.7 V vs. RHE, being more superior than most of the non-noble metal oxide electrocatalysts reported on NO_3RR so far. This work inspires the synergistic effect of asymmetric O_v and ion clusters in promoting NO_3RR performance and provides new insights in engineering the local environment around active sites for highly efficient electrocatalysts.

CRediT authorship contribution statement

Dong Chen conceived the idea and wrote the manuscript. **Dong Chen, Shaoce Zhang, Xiuming Bu, Rong Zhang, Quan Quan, Zhengxun Lai, Wei Wang, You Meng, Di Yin and SenPo Yi** conducted the material synthesis, characterization, NO_3RR measurements and electrochemical test. **Dong Chen, Shaoce Zhang, Rong Zhang** carried out the DFT calculation. **Chuntai Liu, Chunyi Zhi and Johnny C. Ho** directed the research and edit the manuscript.

Declaration of Competing Interest

The authors declare that they have no known competing financial interests or personal relationships that could have appeared to influence the work reported in this paper.

Acknowledgments

This work is supported by the Environment and Conservation Fund of Hong Kong SAR, China (Grant No. ECF 2020-13), a fellowship award from the Research Grants Council of the Hong Kong SAR, China (CityU RFS2021-1S04), the Foshan Innovative and Entrepreneurial Research Team Program (Grant No. 2018IT100031) and the City University of Hong Kong (Project No. 9667227).

Appendix A. Supplementary material

Supplementary data associated with this article can be found in the online version at doi:10.1016/j.nanoen.2022.107338.

References

[1] J.G. Chen, R.M. Crooks, L.C. Seefeldt, K.L. Bren, R.M. Bullock, M.Y. Darensbourg, P.L. Holland, B. Hoffman, M.J. Janik, A.K. Jones, Beyond fossil fuel–driven nitrogen transformations, Science 360 (2018).

[2] J.O. Lundberg, E. Weitzberg, J.A. Cole, N. Benjamin, Nitrate, bacteria and human health, Nat. Rev. Microbiol. 2 (2004) 593–602.

[3] N.E. Ostrom, L.O. Hedin, J.C. Von Fischer, G.P. Robertson, Nitrogen transformations and NO_3^- removal at a soil–stream interface: a stable isotope approach, Ecol Appl. 12 (2002) 1027–1043.

[4] F. Jiao, B. Xu, Electrochemical ammonia synthesis and ammonia fuel cells, Adv. Mater. 31 (2019) 1805173.

[5] C. Smith, A.K. Hill, L. Torrente-Murciano, Current and future role of Haber–Bosch ammonia in a carbon-free energy landscape, Energy Environ. Sci. 13 (2020) 331–344.

[6] B.H. Suryanto, H.-L. Du, D. Wang, J. Chen, A.N. Simonov, D.R. MacFarlane, Challenges and prospects in the catalysis of electroreduction of nitrogen to ammonia, Nat. Catal. 2 (2019) 290–296.

[7] Y. Zeng, C. Priest, G. Wang, G. Wu, Restoring the nitrogen cycle by electrochemical reduction of nitrate: progress and prospects, Small Methods 4 (2020) 2000672.

[8] A. Stirling, I. Pápai, J. Mink, D.R. Salahub, Density functional study of nitrogen oxides, J Chem Phys. 100 (1994) 2910–2923.

[9] P.H. van Langevelde, I. Katsounaros, M.T.M. Koper, Electrocatalytic nitrate reduction for sustainable ammonia production, Joule 5 (2021) 290–294.

[10] H. Yu, F. Chen, X. Li, H. Huang, Q. Zhang, S. Su, K. Wang, E. Mao, B. Mei, G. Mul, Synergy of ferroelectric polarization and oxygen vacancy to promote CO_2 photoreduction, Nat. Commun. 12 (2021) 1–10.

[11] C. Mao, J. Wang, Y. Zou, G. Qi, J.Y. Yang Loh, T. Zhang, M. Xia, J. Xu, F. Deng, M. Ghoussoub, Hydrogen spillover to oxygen vacancy of $TiO_{2-x}H_y$/Fe: breaking the scaling relationship of ammonia synthesis, J. Am. Chem. Soc. 142 (2020) 17403–17412.

[12] C. Feng, L. Tang, Y. Deng, J. Wang, Y. Liu, X. Ouyang, Z. Chen, H. Yang, J. Yu, J. Wang, Maintaining stable LSPR performance of $W_{18}O_{49}$ by protecting its oxygen vacancy: a novel strategy for achieving durable sunlight driven photocatalysis, Appl. Catal. B 276 (2020), 119167.

[13] Y. Ding, L. Huang, J. Zhang, A. Guan, Q. Wang, L. Qian, L. Zhang, G. Zheng, Ru-doped, oxygen-vacancy-containing CeO_2 nanorods toward N_2 electroreduction, J. Mater. Chem. 8 (2020) 7229–7234.

[14] Y. Tang, H. Shen, J. Cheng, Z. Liang, C. Qu, H. Tabassum, R. Zou, Fabrication of oxygen-vacancy abundant NiMn-layered double hydroxides for ultrahigh capacity supercapacitors, Adv. Funct. Mater. 30 (2020) 1908223.

[15] E.W. McFarland, H. Metiu, Catalysis by doped oxides, Chem. Rev. 113 (2013) 4391–4427.

[16] J.B. Pan, B.H. Wang, J.B. Wang, H.Z. Ding, W. Zhou, X. Liu, J.R. Zhang, S. Shen, J. K. Guo, L. Chen, Activity and stability boosting of an oxygen-vacancy-rich $BiVO_4$ photoanode by NiFe-MOFs thin layer for water oxidation, Angew. Chem. Int. Ed. 133 (2021) 1453–1460.

[17] K. Yu, L.L. Lou, S. Liu, W. Zhou, Asymmetric oxygen vacancies: the intrinsic redox active sites in metal oxide catalysts, Adv. Sci. 7 (2020) 1901970.

[18] A.J. Medford, A. Vojvodic, J.S. Hummelshøj, J. Voss, F. Abild-Pedersen, F. Studt, T. Bligaard, A. Nilsson, J.K. Nørskov, From the Sabatier principle to a predictive theory of transition-metal heterogeneous catalysis, J. Catal. 328 (2015) 36–42.

[19] X.-X. Li, D. Zhao, S.-T. Zheng, Recent advances in POM-organic frameworks and POM-organic polyhedra, Coord. Chem. Rev. 397 (2019) 220–240.

[20] Y. Yang, Y. Qian, H. Li, Z. Zhang, Y. Mu, D. Do, B. Zhou, J. Dong, W. Yan, Y. Qin, O-coordinated W-Mo dual-atom catalyst for pH-universal electrocatalytic hydrogen evolution, Sci. Adv 6 (2020) eaba6586.

[21] X. Wang, S. Qiu, J. Feng, Y. Tong, F. Zhou, Q. Li, L. Song, S. Chen, K.H. Wu, P. Su, Confined Fe-Cu clusters as sub-nanometer reactors for efficiently regulating the electrochemical nitrogen reduction reaction, Adv. Mater. 32 (2020) 2004382.

[22] N. Khomutov, U. Stamkulov, Nitrate reduction at various metal electrodes, Sov. Electrochem. 7 (1971) 312–316.

[23] H. Han, S. Jin, S. Park, Y. Kim, D. Jang, M.H. Seo, W.B. Kim, Plasma-induced oxygen vacancies in amorphous MnO_x boost catalytic performance for electrochemical CO_2 reduction, Nano Energy 79 (2021), 105492.

[24] K. Yu, D. Lei, Y. Feng, H. Yu, Y. Chang, Y. Wang, Y. Liu, G.-C. Wang, L.-L. Lou, S. Liu, The role of Bi-doping in promoting electron transfer and catalytic performance of Pt/3DOM-$Ce_{1-x}Bi_xO_{2-\delta}$, J. Catal. 365 (2018) 292–302.

[25] E. Souza, J. Sczancoski, I. Nogueira, M. Almeida, M. Orlandi, M. Li, R. Luz, E. Longo, L. Cavalcante, Structural evolution, growth mechanism and photoluminescence properties of $CuWO_4$ nanocrystals, Ultrason. Sonochem. 38 (2017) 256–270.

[26] X.W. Lou, L.A. Archer, Z. Yang, Hollow micro-/nanostructures: synthesis and applications, Adv. Mater. 20 (2008) 3987–4019.

[27] L. Xiu, W. Pei, S. Zhou, Z. Wang, P. Yang, J. Zhao, J. Qiu, Multilevel hollow MXene tailored low-Pt catalyst for efficient hydrogen evolution in full-pH range and seawater, Adv. Funct. Mater. 30 (2020) 1910028.

[28] K. Chu, J. Wang, Y.-p. Liu, Y.-b Li, C.-c. Jia, H. Zhang, Creating defects on graphene basal-plane toward interface optimization of graphene/CuCr composites, Carbon 143 (2019) 85–96.

[29] K. Chu, J. Wang, Y.-p. Liu, Q.-q. Li, Y.-l. Guo, Mo-doped SnS_2 with enriched S-vacancies for highly efficient electrocatalytic N_2 reduction: the critical role of the Mo–Sn–Sn trimer, J. Mater. Chem. 8 (2020) 7117–7124.

[30] J. Yang, S. Hu, Y. Fang, S. Hoang, L. Li, W. Yang, Z. Liang, J. Wu, J. Hu, W. Xiao, Oxygen vacancy promoted O_2 activation over perovskite oxide for low-temperature CO oxidation, ACS Catal. 9 (2019) 9751–9763.

[31] Z. Xiao, Y.-C. Huang, C.-L. Dong, C. Xie, Z. Liu, S. Du, W. Chen, D. Yan, L. Tao, Z. Shu, Operando identification of the dynamic behavior of oxygen vacancy-rich Co_3O_4 for oxygen evolution reaction, J. Am. Chem. Soc. 142 (2020) 12087–12095.

[32] X. Bi, G. Du, A. Kalam, D. Sun, Y. Yu, Q. Su, B. Xu, A.G. Al-Sehemi, Tuning oxygen vacancy content in TiO_2 nanoparticles to enhance the photocatalytic performance, Chem. Eng. Sci. 234 (2021), 116440.

[33] W. Guo, Y. Wang, X. Lian, Y. Nie, S. Tian, S. Wang, Y. Zhou, G. Henkelman, Insights into the multiple effects of oxygen vacancies on $CuWO_4$ for photoelectrochemical water oxidation, Catal. Sci. Technol. 10 (2020) 7344–7351.

[34] Y. Bo, H. Wang, Y. Lin, T. Yang, R. Ye, Y. Li, C. Hu, P. Du, Y. Hu, Z. Liu, Altering hydrogenation pathways in photocatalytic nitrogen fixation by tuning local electronic structure of oxygen vacancy with dopant, Angew. Chem. Int. Ed. (2021).

[35] L. Wang, X. Duan, X. Liu, J. Gu, R. Si, Y. Qiu, Y. Qiu, D. Shi, F. Chen, X. Sun, Atomically dispersed Mo supported on metallic Co_9S_8 nanoflakes as an advanced noble-metal-free bifunctional water splitting catalyst working in universal pH conditions, Adv. Energy Mater. 10 (2020) 1903137.

[36] Z. Chen, Y. Song, J. Cai, X. Zheng, D. Han, Y. Wu, Y. Zang, S. Niu, Y. Liu, J. Zhu, Tailoring the d-band centers enables Co_4N nanosheets to be highly active for hydrogen evolution catalysis, Angew. Chem. Int. Ed. 130 (2018) 5170–5174.

[37] J. Gonzalez, G. Rivas, S. Mota, D. Brondino, I. Moura, J.G. Moura, Periplasmic nitrate reductases and formate dehydrogenases: biological control of the chemical properties of Mo and W for fine tuning of reactivity, substrate specificity and metabolic role, Coord. Chem. Rev. 257 (2013) 315–331.

[38] Y. Ma, T. Yang, H. Zou, W. Zang, Z. Kou, L. Mao, Y. Feng, L. Shen, S.J. Pennycook, L. Duan, Synergizing Mo single atoms and Mo_2C nanoparticles on CNTs synchronizes selectivity and activity of electrocatalytic N_2 reduction to ammonia, Adv. Mater. 32 (2020) 2002177.

[39] W. Ding, X. Wu, Q. Lu, Structure and photocatalytic activity of thin-walled $CuWO_4$ nanotubes: an experimental and DFT study, Mater. Lett. 253 (2019) 323–326.

[40] Y. Guo, R. Zhang, S. Zhang, Y. Zhao, Q. Yang, Z. Huang, B. Dong, C. Zhi, Pd doping-weakened intermediate adsorption to promote electrocatalytic nitrate reduction on TiO_2 nanoarrays for ammonia production and energy supply with zinc–nitrate batteries, Energy Environ. Sci. 14 (2021) 3938–3944.

[41] S. Garcia-Segura, M. Lanzarini-Lopes, K. Hristovski, P. Westerhof, Electrocatalytic reduction of nitrate: fundamentals to full-scale water treatment applications, Appl. Catal. B 236 (2018) 546–568.

[42] G.-F. Chen, Y. Yuan, H. Jiang, S.-Y. Ren, L.-X. Ding, L. Ma, T. Wu, J. Lu, H. Wang, Electrochemical reduction of nitrate to ammonia via direct eight-electron transfer using a copper–molecular solid catalyst, Nat. Energy 5 (2020) 605–613.

[43] L. Han, X. Liu, J. Chen, R. Lin, H. Liu, F. Lü, S. Bak, Z. Liang, S. Zhao, E. Stavitski, Atomically dispersed molybdenum catalysts for efficient ambient nitrogen fixation, Angew. Chem. Int. Ed. 131 (2019) 2343–2347.

[44] C. Choi, S. Back, N.-Y. Kim, J. Lim, Y.-H. Kim, Y. Jung, Suppression of hydrogen evolution reaction in electrochemical N_2 reduction using single-atom catalysts: a computational guideline, ACS Catal. 8 (2018) 7517–7525.

[45] X. Deng, Y. Yang, L. Wang, X.Z. Fu, J.L. Luo, Metallic Co nanoarray catalyzes selective NH_3 production from electrochemical nitrate reduction at current densities exceeding 2 A cm^{-2}, Adv. Sci. 8 (2021) 2004523.

[46] G.H. An, J. Hong, S. Pak, Y. Cho, S. Lee, B. Hou, S. Cha, 2D metal Zn nanostructure electrodes for high-performance Zn ion supercapacitors, Adv. Energy Mater. 10 (2020) 1902981.

[47] Y.-W. Lee, B.-S. Kim, J. Hong, H. Choi, H.-S. Jang, B. Hou, S. Pak, J. Lee, S.-H. Lee, S.M. Morris, Hierarchically assembled tubular shell-core-shell heterostructure of hybrid transition metal chalcogenides for high-performance supercapacitors with ultrahigh cyclability, Nano Energy 37 (2017) 15–23.

Dong Chen is currently a Ph.D. candidate in the Department of Materials Science and Engineering at the City University of Hong Kong. She received her BS and MS degree from the Tianjin Chengjian University in 2016 and 2019, respectively. Her research interests mainly focus on the design and fabrication of nanomaterials and the application in electrochemical catalysis, etc.

Quan Quan is currently a Ph.D. candidate in the Department of Materials Science and Engineering at the City University of Hong Kong. Her research interests mainly focus on the synthesis of nano-structural catalysts for applications in electrocatalysis and related interdisciplinary sustainable chemistry.

Zhengxun Lai is currently a Ph.D. candidate in the Department of Materials Science and Engineering at the City University of Hong Kong. He received his BSc and MS degree from the Tianjin University in 2016 and 2019, respectively. His research interests mainly focus on the halide perovskites electronic and photoelectric devices, etc.

Wei Wang is currently a Ph.D. candidate in the Department of Materials Science and Engineering at the City University of Hong Kong. He received his BS degree in Electronic Science and Technology form Anhui Jianzhu University in 2012 and MS degree in Materials Engineering from Tongji University in 2015. His research mainly involves the fabrication of nanomaterials, including III-V semiconductor nanowires and 2D materials, along with nanomaterials-based devices regarding the integration of field-effect transistors and near-infrared photoconductors/photodiodes, etc.

You Meng is working as a postdoctoral researcher in the Department of Materials Science and Engineering at the City University of Hong Kong. He received his BS and MS degree in Physics from the Qingdao University in 2015 and 2018, respectively, and a Ph.D. degree in Materials Science and Engineering from the City University of Hong Kong in 2021. His research interests mainly focus on nanomaterials-based neuromorphic electronics, photoconductive/photovoltaic photodetectors, field-effect/electrochemical transistors, etc.

Di Yin is currently a Ph.D. candidate in the Department of Materials Science and Engineering at the City University of Hong Kong. She received her BS degree from Jiangsu University in 2017 and an MS degree from East China University of Science and Technology University in 2020. Her research interests mainly focus on the design and synthesis of nanomaterials and their application for removal of pollutants from the environment, etc.

Johnny C. Ho is a Professor of Materials Science and Engineering at the City University of Hong Kong. He received his BS degree in Chemical Engineering and his MS and Ph.D. degrees in Materials Science and Engineering from the University of California, Berkeley, in 2002, 2005, and 2009, respectively. From 2009 to 2010, he was a postdoctoral research fellow in the Nanoscale Synthesis and Characterization Group at Lawrence Livermore National Laboratory. His research interests focus on synthesis, characterization, integration, and device applications of nanoscale materials for various technological applications, including nanoelectronics, sensors, and energy harvesting.